

A data-driven approach for modeling large-amplitude aeroelastic oscillations of pitching wings

Yuanhang Zhu^{a,1,*}, Kenneth Breuer^a

^aCenter for Fluid Mechanics, School of Engineering, Brown University, Providence, RI, 02912, USA

Abstract

We propose and validate a data-driven approach for modeling large-amplitude flow-induced oscillations of elastically mounted pitching wings. We first train a neural networks regression model for the nonlinear aerodynamic moment using data obtained from purely prescribed oscillations and static measurements. We then embed this model into an ordinary differential equation solver to solve for the governing equation of the passive aeroelastic system with desired structural parameters. The system dynamics predicted by the proposed data-driven method are characterized and compared with those obtained from physical experiments. The predicted and experimental pitching amplitude, frequency and aerodynamic moment responses are found to be in excellent agreement. Both the structural mode of high-inertia wings and the hydrodynamic mode of low-inertia wings are successfully predicted. The transient growth and saturation of the oscillation amplitude and the aerodynamic moment are also faithfully captured by the proposed method. Additional test cases demonstrate the broad applicability of this approach.

Keywords:

Fluid-Structure Interaction, Aeroelasticity, Unsteady Aerodynamics, Neural Networks, Machine Learning

1. Introduction

The interactions between free-stream flows and elastically supported structures can lead to large-amplitude self-sustained oscillations, such as vortex-induced vibrations of cylinders (Williamson and Govardhan, 2004; Gabbai and Benaroya, 2005; Williamson and Govardhan, 2008) and aeroelastic instabilities of airfoils (Dowell et al., 1989; Dowell and Hall, 2001; Dowell et al., 2003; Dimitriadis and Li, 2009; Dimitriadis, 2017). These flow-induced oscillations can pose severe risks, potentially leading to structural failure in extreme conditions (Larsen, 1998), but they also present opportunities for hydrokinetic energy harvesting from river or tidal flows (Xiao and Zhu,

*Corresponding author

Email address: yuanhang_zhu@alumni.brown.edu (Yuanhang Zhu)

¹Present address: Department of Mechanical and Aerospace Engineering, University of Virginia, Charlottesville, VA 22904, USA

2014; Young et al., 2014; Onoue et al., 2015; Su and Breuer, 2019; Wang et al., 2020), providing alternative solutions for renewable energy generation.

To comprehensively understand and effectively control these complex flow-induced oscillations, numerous efforts have been made to study the corresponding fluid-structure interactions (FSI) using reduced-order models. One common way of simplifying a high degrees-of-freedom aeroelastic system is to model it as a spring-mass-damper system subjected to nonlinear fluid forcing (Khalak and Williamson, 1996; Dugundji, 2008). In the present study, we consider an aeroelastic system with a pitching degree of freedom:

$$I\ddot{\theta} + b\dot{\theta} + k\theta = M, \quad (1)$$

where θ , $\dot{\theta}$, $\ddot{\theta}$ are pitching angle, velocity, acceleration, I , b , k are wing inertia, damping, stiffness, and M is the aerodynamic moment. While the left-hand-side spring-mass-damper system is relatively easy to simulate, the fluid forcing term on the right-hand side, which mainly results from the formation and shedding of vortices around the bluff body, is often found to be highly nonlinear and difficult to model and predict. This second-order ordinary differential equation can be solved numerically if the unsteady fluid forcing term, M , can be modeled as a function of the instantaneous system kinematics and flow parameters:

$$M = \mathcal{F}(\theta, \dot{\theta}, \ddot{\theta}, Re, \dots), \quad (2)$$

where Re is the Reynolds number. Several other parameters, such as geometry and surface roughness, may also be important.

Classic models from Theodorsen (1935) and Garrick (1936) provide an analytical solution for estimating the unsteady aerodynamic forces on two-dimensional airfoils undergoing harmonic oscillations. However, these linear models are based on potential flow theory assuming a thin airfoil, and are only applicable to attached flows and small-amplitude oscillations. To what extent do these models apply to highly separated, vortex-dominated flows and large-amplitude oscillations remains an active research direction (McCroskey, 1982; Baik et al., 2012; Liu et al., 2015; Ōtomo et al., 2021). Vortex-based models have been proposed thereafter to incorporate the unsteady effect of shed vortices (Clements and Maull, 1975; Katz, 1981; Xia and Mohseni, 2013; Wang and Eldredge, 2013; Ramesh et al., 2014), as reviewed by Eldredge and Jones (2019). These models provide valuable tools for predicting aerodynamic forces in highly separated flows, capturing the essential physics with lower computational cost than full numerical simulations. However, their accuracy in extreme conditions may still be limited, and careful validation against experimental or high-fidelity numerical data is necessary. Ford and Babinsky (2013) proposed a semi-empirical model that combines potential flow theory with experimentally determined vortex position and strength. This approach was later adapted by Onoue and Breuer (2016) to model the unsteady aerodynamic load of pitching wings undergoing large-amplitude flow-induced oscillations. Although these semi-empirical models were successful, they require additional velocity field information, which might not be practical for real-time aeroelastic simulations.

The low-order analytical and semi-empirical models discussed above have good “interpretability”, in that the unsteady aerodynamic load can be associated with the corresponding flow physics,

such as variations of leading-edge suction and vortex shedding. However, when it comes to real-time predictions of the overall dynamics of aeroelastic systems, the interpretability of the unsteady fluid forcing term becomes less critical.

Modeling the “two-way” coupling between the fluid and the structure using high-fidelity numerical simulations (e.g. Goza and Colonius (2017); Menon and Mittal (2019)) is nontrivial and computationally expensive, and not practical for real-time aeroelastic predictions. In contrast, it is substantially easier to implement fluid-structure interactions with “one-way” coupling - prescribing the structural motion and measuring or simulating the fluid response. As such, it is of great practical value to develop and to test an unsteady fluid forcing model based on one-way coupling FSI and to integrate this model into two-way coupling scenarios. In fact, previous studies have shown that large-amplitude flow-induced oscillations are largely sinusoidal, and with this observation, an “energy method” has been used to accurately characterize two-way aeroelastic oscillations using one-way prescribed oscillations (Morse and Williamson, 2009; Bhat and Govardhan, 2013; Menon and Mittal, 2019; Zhu et al., 2020). The energy method uses prescribed sinusoidal motions (one-way coupling) to map out the cycle-averaged energy transfer between the ambient fluid and the elastic structure over a large range of oscillating frequencies and amplitudes. The stability of the passive aeroelastic system (two-way coupling) can thus be inferred from the energy transfer, as the energy injected by the ambient fluid should always balance the energy dissipated by the structural damping for self-sustained oscillations. However, this approach is only capable of predicting the *overall* stability of passive systems and the *cycle-averaged* amplitude and frequency of self-sustained flow-induced oscillations. It is not able to make predictions for the *instantaneous* dynamics of the system, such as the bifurcation points, the transitional dynamics, and the mode of oscillations, because the energy transfer is evaluated in a cycle-averaged manner.

With the rapid development of machine learning tools in fluid mechanics (Brunton et al., 2016; Brenner et al., 2019; Raissi et al., 2019; Brunton et al., 2020; Kou and Zhang, 2021; Menon and Mittal, 2021; Lee et al., 2022; Siddiqui et al., 2022; Mishra et al., 2023; Ribeiro and Franck, 2023; Hickner et al., 2023; Fukami and Taira, 2023; Graff et al., 2023; Chen et al., 2023; Carter and Ganapathisubramani, 2023), we see a possibility of better bridging one-way and two-way coupling FSI problems and substantially reducing the experimental and computational costs of studying nonlinear aeroelastic systems. In the present study, we propose a data-driven approach to model large-amplitude aeroelastic oscillations of pitching wings. Our approach uses data obtained from prescribed (one-way coupling) experiments to train a machine-learning regression model. We then combine the trained model with the aeroelastic governing equation and simulate the real-time aeroelastic dynamics (two-way coupling) by solving the governing equation based on the desired structural parameters. In the following sections, we will first introduce our mythology (§2), including the experimental and machine learning setup (§2.1), as well as the data assembling (§2.2), training (§2.3), and validation (§2.4) steps. This is followed by comparing the results obtained from the data-driven approach with fully two-way aeroelastic experimental measurements (§3). Finally, we discuss the results and summarize all the key findings in §4.

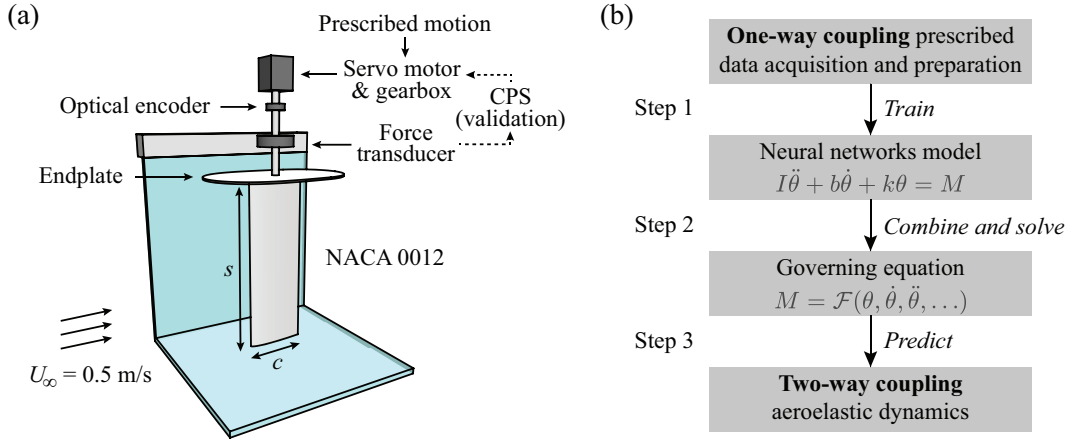


Figure 1: (a) A schematic of the experimental setup. (b) A flow chart of the proposed data-driven approach.

2. Methods

2.1. Experimental setup and machine learning workflow

As we discussed in the previous section, the goal of the present work is to propose a data-driven approach to bridge one-way and two-way coupling fluid-structure interaction problems and use the approach to model large-amplitude aeroelastic oscillations. To achieve this goal, we first conduct prescribed-motion experiments to obtain the training data. A schematic of the experimental setup is shown in Fig. 1(a). We mount a NACA 0012 wing vertically in a circulating free-surface water tunnel (test section $W \times D \times L = 0.8 \text{ m} \times 0.6 \text{ m} \times 4.0 \text{ m}$). The wing has a chord length of $c = 0.1 \text{ m}$ and a span of $s = 0.3 \text{ m}$. An endplate is attached to the wing root to skim surface waves and eliminate tip vortices. The endplate also acts as a symmetry plane, resulting in an effective aspect ratio of $AR = 6$. As we will show later, the specific geometry of the wing (e.g. pitching axis, cross-section shape, aspect ratio, sweep angle, endplates, etc) does not affect the effectiveness of the proposed data-driven approach. The free-stream velocity is fixed at $U_\infty = 0.5 \text{ m/s}$, which results in a chord-based Reynolds number of $Re \equiv \rho U_\infty c / \mu = 50,000$, where ρ and μ are water density and dynamic viscosity, respectively.

The wing pitches around a vertical shaft at the mid chord, which is further connected to a six-axis force/moment transducer (ATI 9105-TIF-Delta-IP65), an optical encoder (US Digital E3-2500), and a servo motor (Parker SM233AE) coupled with a 5:1 gearbox (Automation Direct PGCN23-0525). The force/moment transducer measures the aerodynamic moment, M , experienced by the wing and the encoder measures the pitching angle, θ . Both signals are recorded on a desktop computer via a data acquisition (DAQ) board (National Instruments PCIe-6353) at a rate of 1,000 Hz. Note that all the training data acquired for the proposed data-driven approach are from *prescribed* pitching motions or *static* moment measurements (one-way coupling).

Fig. 1(b) shows a flow chart of the proposed data-driven approach. The first step is to acquire and prepare the one-way coupling training data, which will be discussed in detail in the following subsection (§2.2). We then use the prepared data to train a neural networks (NN) model (§2.3). The trained model is later combined with the governing equation to make predictions of the dynamics

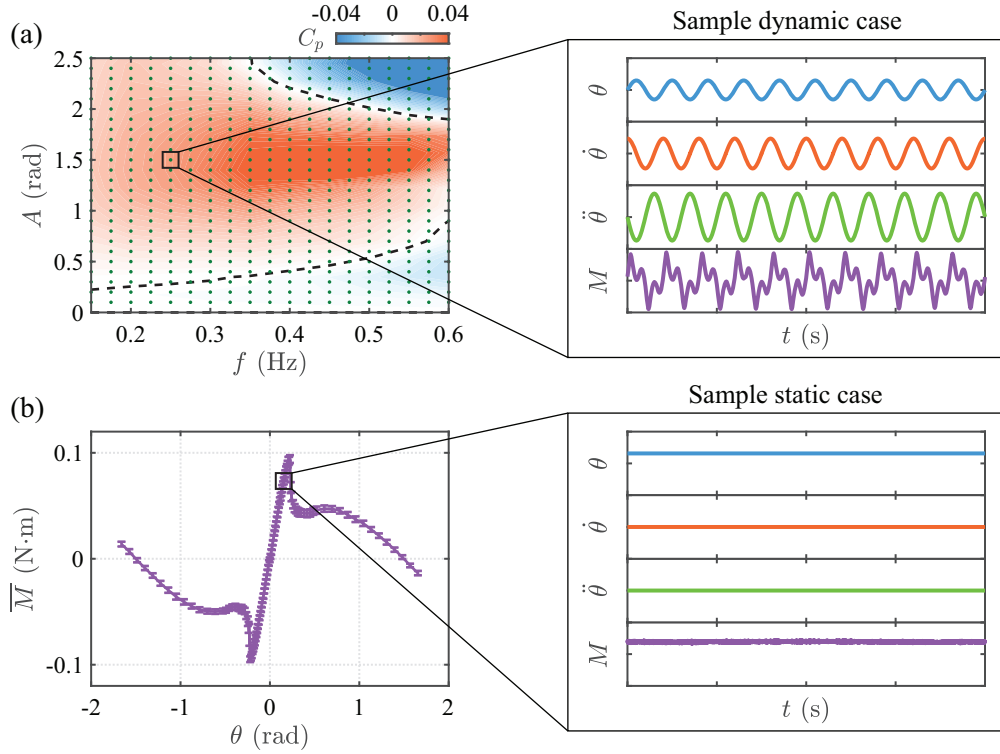


Figure 2: (a) Power transfer map of the system, generated by one-way coupling prescribed sinusoidal motions. Green dots represent the locations of the $i = 475$ data points. Zoom-in window: time series data of the three predictors (θ , $\dot{\theta}$ and $\ddot{\theta}$) and the response (M) for case $A = 1.5$ and $f = 0.25$ Hz. (b) Static aerodynamic moment measurement as a function of the pitching angle ($j = 105$ cases). Zoom-in window: time series of the training data θ , $\dot{\theta}$, $\ddot{\theta}$ and M for case $\theta = 0.157$.

of the two-way coupling aeroelastic system (§2.4).

2.2. Training data acquisition and preparation

The one-way coupling training data contains two parts. The first part is the *dynamic* data acquired from prescribed sinusoidal oscillations and the second part is the *static* data obtained from static aerodynamic moment measurements. Fig. 2(a) and (b) illustrate how the training data is extracted from the dynamic and static measurements, respectively.

To obtain the dynamic training data, we prescribe sinusoidal pitching motions of the wing using the following equation (Zhu et al., 2020)

$$\theta = A \sin(2\pi f_p t), \quad (3)$$

where A is the pitching amplitude, f_p is the pitching frequency and t is the time. A is varied from 0 to 2.5 rad with a step size of 0.1 rad and f is varied from 0.15 Hz to 0.6 Hz with a step size of 0.025 Hz, resulting in $i = 475$ total prescribed (dynamic) cases. These cases were previously used to construct the power transfer map in Zhu et al. (2020). Here we replot the power transfer map in

Fig. 2(a) without considering structural damping. The power transfer coefficient is calculated as

$$C_p = \frac{f_p^*}{n} \int_{t_0}^{t_0+nT} C_M \dot{\theta}^* dt^*, \quad (4)$$

where $f_p^* = f_p c / U_\infty$ is the non-dimensional pitching frequency, $n = 10$ is the number of pitching cycles, t_0 is the starting time, $T = 1/f_p$ is the pitching period, C_M is the moment coefficient, $\dot{\theta}^* = \dot{\theta} c / U_\infty$ is the non-dimensional pitching velocity, and $t^* = t U_\infty / c$ is the non-dimensional time. On this power transfer map, orange regions represent $C_p > 0$, where more power is being injected into the system from the ambient flow, whereas blue regions represent $C_p < 0$, where more power is being damped into the ambient flow from the system. The black dashed curve represents neutral power transfer, $C_p = 0$, where the system is at an equilibrium state. The green dots on the map represent the locations of the $i = 475$ dynamic cases. The zoom-in window shows the time series data of the pitching angle, θ , the pitching velocity, $\dot{\theta}$, and the pitching acceleration, $\ddot{\theta}$, and the aerodynamic moment, M , measured at the sample case $A = 1.5$ and $f = 0.25$ Hz. The pitching velocity and the pitching acceleration are differentiated from the time-resolved pitching angle. For each prescribed dynamic case, 10 pitching cycles are recorded.

In addition to the dynamic data, the static data is also important for predicting the dynamic of the system, in particular the onset of flow-induced oscillations (Zhu et al., 2020; Zhu and Breuer, 2023). To obtain the static training data, we measure the static pitching moment when the wing is fixed at different angles of attack for $-1.66 \text{ rad} \leq \theta \leq 1.66 \text{ rad}$ with an adaptive step size (0.009 rad near $\theta = 0$ and 0.09 rad near $\theta = \pm 1.66$ rad). The static moment curve is shown in Fig. 2(b). The resultant pitching velocity and pitching acceleration for these static cases are both zero. The zoom-in window shows the corresponding time series data for the sample static case $\theta = 0.157$. In total, $j = 105$ static cases are measured and each measurement lasts 20 seconds. For both the dynamic and the static cases, no filter is applied to the aerodynamic moment data.

After the $i = 475$ dynamic cases and the $j = 105$ static cases are collected, we assemble the $i + j = 580$ cases together to construct the training dataset. A state vector containing four quantities - θ , $\dot{\theta}$, $\ddot{\theta}$, and M - is selected and joined together to form a four-column matrix representing every parameter combination. The $i + j = 580$ cases are shuffled to test for the robustness of the trained model (see Appendix). Table 1 shows how the training dataset is assembled and structured. The assembled data has 3 features - θ , $\dot{\theta}$, and $\ddot{\theta}$ - as ‘‘predictors’’, and the aerodynamic moment, M , as the system ‘‘response’’. The final training dataset is a matrix of 17,029,725 rows and 4 columns. We want to emphasize again that only prescribed and static data (one-way coupling) are used as training data, no passive two-way coupling data are involved.

2.3. Model training

The training dataset is then fed into the MATLAB Regression Learner for training. In this study, we select feed-forward neural networks as our machine-learning regression model. This model is known for being able to process data with high non-linearity (Cybenko, 1989). The neural networks model has three fully connected layers with 10 nodes on each layer. Five-fold cross-validation is used to evaluate the predictive accuracy. The training time on an Intel® Core™ i5-10400F CPU @ 2.90 GHz with 32 GB memory without any GPU is about 8 hours. Fig. 3

| | | | | | | | |
|----------------|----------------|----------------------|-----------------------|----------------------|-----------|-----------------------|----------------|
| Predictors: | θ_{D11} | $\dot{\theta}_{D11}$ | $\ddot{\theta}_{D11}$ | Response: | M_{D11} | } | Dynamic case 1 |
| | θ_{D12} | $\dot{\theta}_{D12}$ | $\ddot{\theta}_{D12}$ | | M_{D12} | | |
| | θ_{D13} | $\dot{\theta}_{D13}$ | $\ddot{\theta}_{D13}$ | | M_{D13} | | |
| | \vdots | \vdots | \vdots | | \vdots | | |
| | θ_{D21} | $\dot{\theta}_{D21}$ | $\ddot{\theta}_{D21}$ | | M_{D21} | } | Dynamic case 2 |
| | θ_{D22} | $\dot{\theta}_{D22}$ | $\ddot{\theta}_{D22}$ | | M_{D22} | | |
| | θ_{D23} | $\dot{\theta}_{D23}$ | $\ddot{\theta}_{D23}$ | | M_{D23} | | |
| | \vdots | \vdots | \vdots | | \vdots | | |
| | \dots | \dots | \dots | | \dots | Dynamic case 3 to i | |
| | θ_{S11} | 0 | 0 | | M_{S11} | } | Static case 1 |
| | θ_{S12} | 0 | 0 | | M_{S12} | | |
| | θ_{S13} | 0 | 0 | | M_{S13} | | |
| | \vdots | \vdots | \vdots | | \vdots | | |
| | θ_{S21} | 0 | 0 | | M_{S21} | } | Static case 2 |
| | θ_{S22} | 0 | 0 | | M_{S22} | | |
| θ_{S23} | 0 | 0 | M_{S23} | | | | |
| \vdots | \vdots | \vdots | \vdots | | | | |
| \dots | \dots | \dots | \dots | Static case 3 to j | | | |

Table 1: Training data structure.

shows a schematic of the neural networks structure used in the present study. We use three first-order features (θ , $\dot{\theta}$, and $\ddot{\theta}$) to train the machine learning model for the aerodynamic moment $M = (\theta, \dot{\theta}, \ddot{\theta})$. In a separate test (not shown), we have included the second-order features (i.e. θ^2 , $\dot{\theta}^2$, $\ddot{\theta}^2$, $\theta\dot{\theta}$, $\theta\ddot{\theta}$ and $\dot{\theta}\ddot{\theta}$) and no significant improvements of the model performance were observed.

2.4. Aeroelastic response prediction and validation

To make predictions for the aeroelastic response, we embed the trained aerodynamic moment model $M = (\theta, \dot{\theta}, \ddot{\theta})$ into the governing equation of the aeroelastic system (Eq. 1). We use a customized Fourth Order Runge–Kutta (RK4) solver to solve the governing equation. The MATLAB ode45 function is not applicable to this problem because of its adaptive step size. The inertia, I , the structure damping, b , and the torsional stiffness, k , can be assigned to desired values to mimic physical experiments. For each combination of I , b , and k (i.e. each simulation case), we solve Eq. 1 with a step size of 1/100 s and a duration of 120 seconds. At t_0 , we assign initial values for θ_0 , $\dot{\theta}_0$ and $\ddot{\theta}_0$. Based on these initial values, we obtain the aerodynamic moment at the first time step, M_1 , using the trained machine learning model. This M_1 is then fed into the RK4 solver to solve for θ_1 , $\dot{\theta}_1$ and $\ddot{\theta}_1$ at the next time step t_1 . This loop continues until the time limit is reached (120 seconds for each case). The values of θ , $\dot{\theta}$ and $\ddot{\theta}$ at the last time step of the current case are used as the initial condition for the next case. For each case, the kinematics of the system (θ , $\dot{\theta}$ and $\ddot{\theta}$) as well as the aerodynamic moment (M) are collected as time series data for further analysis. This iteration loop is reflected on the right side of Fig. 3.

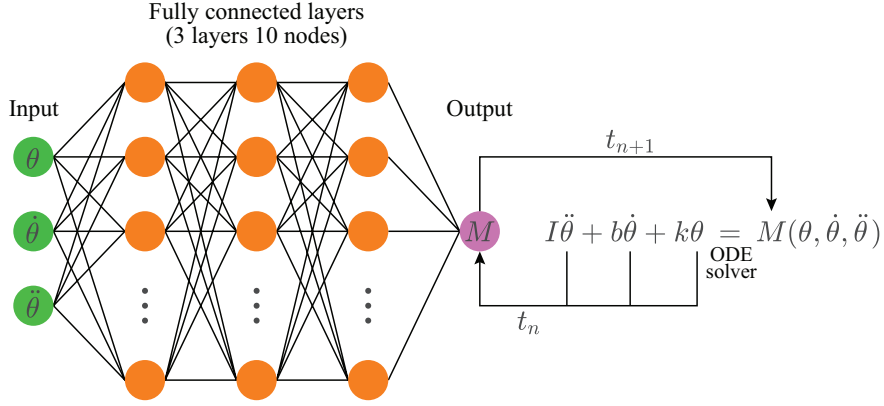


Figure 3: A schematic showing the neural networks structure and how the trained model is integrated with the governing equation to simulate the instantaneous aeroelastic response.

In the present study, we fix the wing inertia, I , and the structural damping, b , and vary the torsional stiffness, k , resembling the bifurcation tests in physical experiments (Onoue et al., 2015; Zhu et al., 2020; Zhu and Breuer, 2023). Following previous experiments, we normalize the governing equation Eq. 1 using the fluid inertia to get the non-dimensional governing equation of the system:

$$I^* \ddot{\theta}^* + b^* \dot{\theta}^* + k^* \theta^* = C_M, \quad (5)$$

where

$$\theta^* = \theta, \quad \dot{\theta}^* = \frac{\dot{\theta}c}{U_\infty}, \quad \ddot{\theta}^* = \frac{\ddot{\theta}c^2}{U_\infty^2}, \quad I^* = \frac{I}{0.5\rho c^4 s}, \quad b^* = \frac{b}{0.5\rho U_\infty c^3 s}, \quad k^* = \frac{k}{0.5\rho U_\infty^2 c^2 s}, \quad C_M = \frac{M}{0.5\rho U_\infty^2 c^2 s}. \quad (6)$$

Here I^* , b^* , k^* and C_M are non-dimensional inertia, structural damping, torsional stiffness and aerodynamic moment, respectively. In the “virtual” experiments, we use the inverse of the non-dimensional stiffness, or the Cauchy number, $Ca = 1/k^*$, as the control parameter. The amplitude response, A , the frequency response f_p , and the moment response, M , are analyzed to quantify the dynamics of the virtual aeroelastic system.

Results from these “virtual” experiments are compared against those obtained from physical two-way coupling aeroelastic experiments. These physical experiments are conducted using a force-feedback cyber-physical system (CPS, see the dash-line loop in Fig. 1a) (Zhu et al., 2020, 2021; Zhu and Breuer, 2023). The CPS mimics the spring-mass-damper system using a high-bandwidth digital (“cyber”) control loop and at the same time measures the physical aerodynamic load using a force transducer. This type of system has been shown to be effective in studying a variety of fluid-structure interaction problems, and it is well known for its convenience in varying the structural parameters. The CPS allows us to control the mass of the wing and thus the mass ratio of the system (the ratio of the wing inertia to that of the surrounding fluid), and in this way the data acquired in a *water* tunnel can be accurately applied to represent aeroelastic instabilities in *air*. More details of the current CPS setup can be found in Zhu et al. (2020).

3. Results

3.1. Predictions of the system response - structural and hydrodynamic modes

Zhu et al. (2020) discovered two distinct oscillation modes of aeroelastic pitching wings. For a high-inertia wing, the aeroelastic oscillations are dominated by the inertial force, corresponding to a “structural mode” in which high amplitude aeroelastic instability is characterized by a subcritical bifurcation and the oscillation frequency, $f_p^* = f_p c / U_\infty$, is locked into the structural frequency, $f_s^* = c \sqrt{k/I - (b/2I)^2} / (2\pi U_\infty)$. For a low-inertia wing, the aeroelastic oscillations are characterized by a supercritical bifurcation and the oscillation frequency is associated with vortex shedding at a constant Strouhal number, $St = f_p^* \approx 0.09$. They labeled this as a “hydrodynamic mode”. To test if the proposed data-driven approach can accurately reproduce these two oscillation modes, we conduct “virtual” bifurcation tests and compare the results with those obtained from physical experiments (Zhu et al., 2020; Zhu and Breuer, 2023). We choose two wing inertia values, $I^* = 10.6$ (structural mode) and $I^* = 0.66$ (hydrodynamic mode), and fix the structural damping at a small value $b^* = 0.13$. For each wing inertia, we start with a low Cauchy number, Ca (i.e. high spring stiffness, k^*), and incrementally increase Ca (decrease k^*) to test for the onset of large-amplitude limit-cycle oscillations (LCOs). We then decrease Ca (increase k^*) to test for any hysteresis. At each Ca , time traces of the system dynamics (θ , $\dot{\theta}$ and $\ddot{\theta}$) and the aerodynamic moment M are generated using the data-driven approach. To mimic the physical experiments of Zhu et al. (2020), the last value of the state vector for the current Ca is used as the initial condition for the next Ca .

We plot the predicted amplitude response of the system, A (i.e. the pitching amplitude, in radians), as a function of the control parameter, Ca , using orange markers in Fig. 4(a) and (d). Results from the physical aeroelastic experiments are also plotted using blue markers for comparison. As shown in the figures, for both cases, the system first stays at a stable fixed point regime where no oscillations are observed due to the high spring stiffness. As we decrease the stiffness, static divergence and small-amplitude oscillations around the static divergence angle start to emerge. At a Hopf point, the system bifurcates to large-amplitude limit-cycle oscillations. For the high-inertia wing (Fig. 4a), this bifurcation occurs abruptly and the system experiences a jump in amplitude, hallmarking a subcritical bifurcation (Strogatz, 1994). For the low-inertia wing (Fig. 4b), however, the bifurcation is smooth and no amplitude jump is observed, indicating a supercritical bifurcation. For both cases, the amplitude of the oscillations increases as we keep increasing Ca above the Hopf point. We then reverse the operation and decrease Ca . For the high-inertia case ($I^* = 10.6$), the system stays at the large-amplitude LCO regime even when Ca is decreased below the Hopf point. This hysteretic behavior creates a bistable region, which is another indicator of a subcritical bifurcation. Within the bistable region, the system has a stable fixed point solution, a stable LCO solution (i.e. bistability), and an unstable LCO solution (not observable in real experiments nor using the data-driven approach). The system finally falls back to the stable fixed point regime via a saddle-node (SN) point as Ca is further decreased. In contrast, no hysteresis is observed for the low-inertia wing ($I^* = 0.66$) and the system follows exactly the same route back to the stable fixed point regime - again, illustrating a hallmark of a supercritical bifurcation.

Comparing machine-learning results (orange) with experiments (blue), we see that the overall performance of the proposed data-driven approach is excellent. The ML model accurately predicts

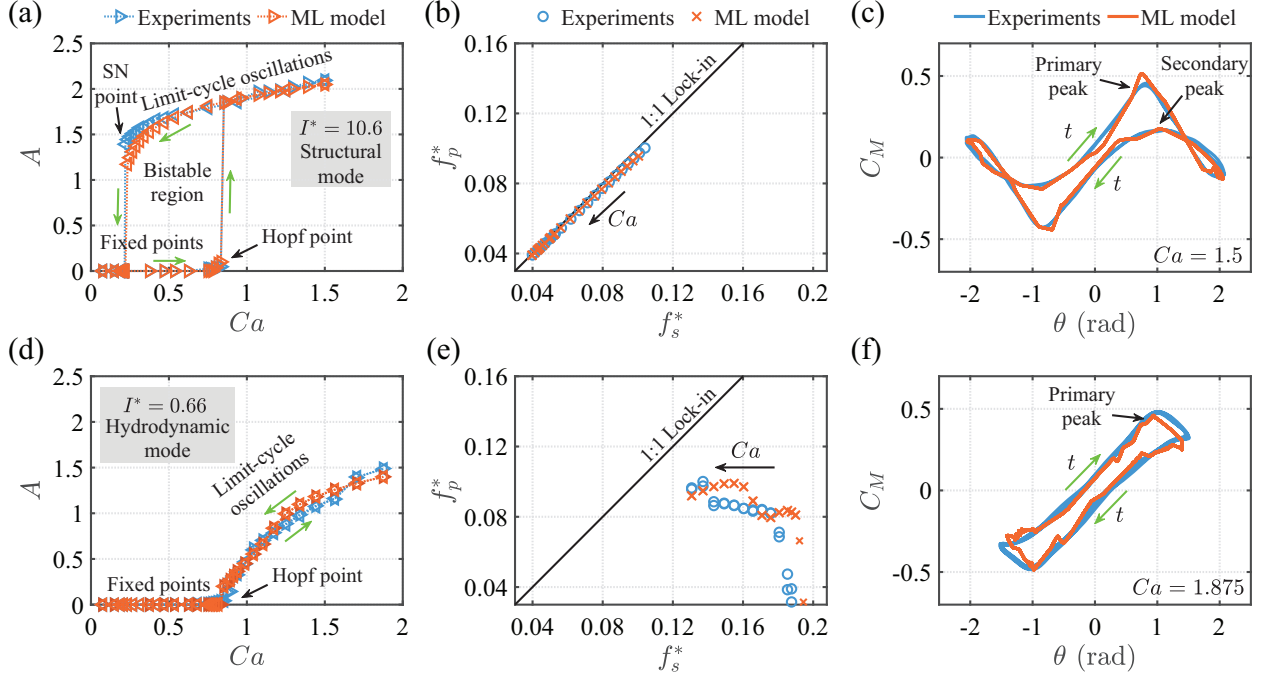


Figure 4: Comparisons between results obtained from the proposed data-driven approach (orange markers) and physical experiments (blue markers). (a-c) A high-inertia wing ($I^* = 10.6$) which corresponds to a *structural* mode. (d-f) A low-inertia wing ($I^* = 0.66$) which corresponds to a *hydrodynamic* mode. (a,d) The amplitude response (bifurcation diagrams). (b,e) The frequency response. (c,f) The pitching angle-aerodynamic moment phase portrait.

the dynamical characteristics of the aeroelastic system for both the high-inertia structural mode and the low-inertia hydrodynamic mode. The two types of bifurcations (subcritical and supercritical) are faithfully reproduced with accurate prediction of the bifurcation points. The LCO amplitude of the machine-learning model also matches well with experiments, despite small discrepancies near the saddle-node point for the high-inertia case (Fig. 4a).

Fig. 4(b) and (e) show the frequency response of the system, where the measured pitching frequency, f_p^* is plotted against the natural (structural) frequency, f_s^* . For the high-inertia wing (Fig. 4b), f_p^* locks on to f_s^* , indicating a structural oscillation mode, where the oscillations are dominated by the inertia force (Zhu et al., 2020). The pitching frequency predicted by the data-driven approach matches very well with experiments. The slight divergence between the frequency response and the 1:1 lock-in line, which is presumably caused by the added-mass effect (Zhu et al., 2020), is also accurately reflected in the ML model. Since the full aerodynamic moment (M) was used as the training data, this includes the added-mass contributions, thus this effect is incorporated into the neural networks predictions. For the low-inertia wing (Fig. 4e), as we increase Ca , the measured pitching frequency f_p remains relatively constant and stays below the 1:1 lock-in value. This shows that the oscillations are dictated by a fluid time scale and thus the fluid force, hallmarking a hydrodynamic mode (Zhu et al., 2020). The ML model faithfully captures the frequency response of this mode, despite a higher discrepancy as compared to the prediction of the structural mode.

Finally, the moment responses of the system (i.e. the moment-angle phase portrait) at the

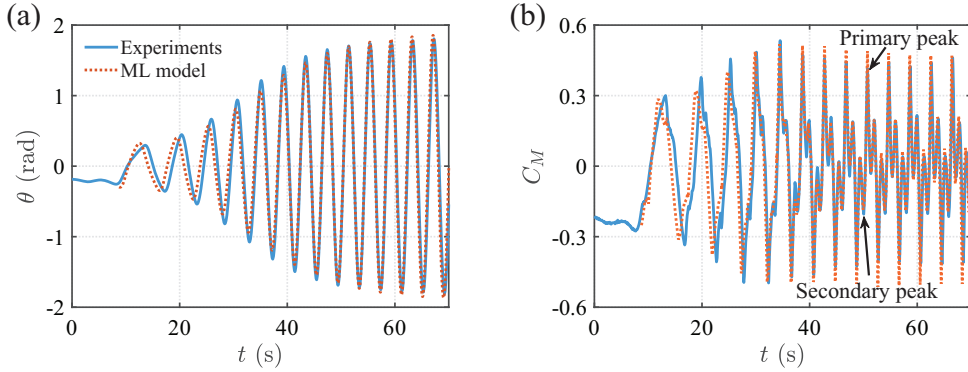


Figure 5: (a) Pitching amplitude transition to large-amplitude limit-cycle oscillations right after the Hopf point for the case $I^* = 10.6$, $b^* = 0.13$, $Ca = 0.85$. (b) The corresponding evolution of the aerodynamic moment.

maximum Cauchy number ($Ca = 1.5$ for $I^* = 10.6$ and $Ca = 1.875$ for $I^* = 0.66$) are shown in Fig. 4(c) and (f). We see that the moment response predicted by the data-driven method agrees well with the experimental results. Zhu et al. (2020) discussed the interpretation of these phase maps and their relation to the vortex dynamics in detail. For the high-inertia wing (Fig. 4c), the primary peak in the moment induced by the formation and shedding of a strong leading-edge vortex (LEV) during the upstroke, as well as the secondary peak induced by a secondary LEV during the pitch reversal, are both accurately captured by the data-driven method. For the low-inertia wing (Fig. 4f), the wing only sheds one LEV during the upstroke. Therefore, only one peak is observed in the phase portrait. The accurate prediction of the aerodynamic moment enables good agreement between the data-driven and the experimental results in the amplitude response (Fig. 4a,d) and the frequency response (Fig. 4b,e).

3.2. Predictions of the unsteady transition dynamics

Another important feature of the aeroelastic system dynamics is the transition of the system from a stable fixed point to large-amplitude limit-cycle oscillations, which occurs as the Cauchy number first rises above its critical value at the bifurcation point (Fig. 4a,d). In particular, it is of great practical importance to characterize the transition after the subcritical Hopf point (Fig. 4a), because the subcritical bifurcation is abrupt and often considered to be dangerous in engineering applications (Strogatz, 1994). Right after the bifurcation point, the system experiences a rapid amplitude growth before saturating into large-amplitude limit-cycle oscillations.

To test if the proposed data-driven method can accurately capture this transition, in Fig. 5, we compare the ML-predicted pitching amplitude and aerodynamic moment as a function of time, with those obtained from experiments. The transition occurs at $I^* = 10.6$, $b^* = 0.13$, $Ca = 0.85$. For better comparisons, the offset of the predicted time trace is adjusted to align with the experimental results. We see that both the amplitude and the aerodynamic moment evolution predicted by the data-driven approach match well with experiments. This excellent agreement is somewhat surprising because we have only used prescribed *periodic* oscillations with *constant* amplitudes and static measurements at *fixed* angles of attack for training the machine learning model; no transition data are included in the training dataset (Table 1). Zhu et al. (2020) reported the emergence of a secondary LEV during the transition to large-amplitude LCOs, which corresponds to an

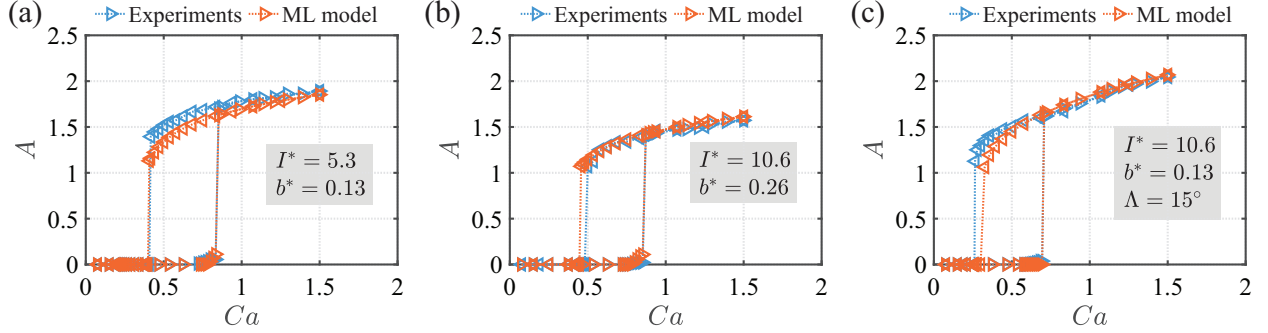


Figure 6: Bifurcation diagram comparisons between experiments and the data-driven approach for additional cases. (a) $I^* = 5.3$ and $b^* = 0.13$ (half the inertia of Fig. 4a). (b) $I^* = 10.6$ and $b^* = 0.26$ (double the damping of Fig. 4a). (c) $I^* = 10.6$ and $b^* = 0.13$ with a leading-edge sweep angle of $\Lambda = 15^\circ$ (requires training a new neural networks model with data taken at $\Lambda = 15^\circ$).

emerging secondary peak in the aerodynamic moment measurement. This process is also faithfully captured by the data-driven method, as depicted in Fig. 5(b). We can see that the amplitude of the secondary peak grows and saturates during the transition. Fig. 5 shows that the machine learning model is able to make good predictions for unsteady dynamics even though it is trained only using steady-state, harmonic data. We believe this success is due to the fact that the time scale associated with the state transition is slow as compared to the time scale of the limit-cycle oscillations. This result is consistent with our previous “ring-down” experiments (Zhu et al., 2021) where we have shown that cycle-averaged values can be used to quantify the slow decay of oscillations due to fluid damping if the transition time scale is slow.

3.3. Performance of the machine-learning model over a range of parameters

To demonstrate the broad applicability of the proposed data-driven approach, we test the ML model on three additional cases, and compare the results with physical experiments in Fig. 6. In Fig. 6(a), we reduce the wing inertia of case Fig. 4(a) to half, which results in $I^* = 5.3$ and $b^* = 0.13$. We see that at this wing inertia, the system still undergoes a subcritical Hopf bifurcation to large-amplitude LCOs, despite a smaller bistable region. The ML model precisely predicts both the Hopf point and the saddle-node point, although it slightly underpredicts the LCO amplitude. In Fig. 6(b), we maintain the same wing inertia as in Fig. 4(a), $I^* = 10.6$, and double the structural damping to $b^* = 0.26$. The LCO amplitude becomes lower at this damping value, but the system still features a subcritical bifurcation and a structural oscillation mode. For this case, the LCO amplitude is precisely predicted by the ML model, but the predicted saddle-node point has a slight discrepancy as compared to experiments. Note that in order to run the cases of Fig. 6(a) and (b), we only need to change the structural parameters in the governing equation (see step 2 in Fig.1b and §2.4). The trained ML model stays the same and no additional data or training is required.

The ML model does have limitations. We note that this ML model does not reproduce the experimental results for extremely small values of wing inertia. For example, we have tested the model with $I^* = 0.33$ (results not shown), and large-amplitude LCOs are not observed for the Ca range tested except at the maximum value, $Ca = 1.875$. Instead, the model predicts the system to have small-amplitude oscillations ($A < 0.3$). The machine-learning model does not allow us

to further investigate the cause of this discrepancy because it is non-interpretable. However, we hypothesize that as the wing inertia becomes too small, the unsteady fluid forcing term becomes dominant, and the “clock” and the dynamics of the aeroelastic system become very sensitive to the exact phase and amplitude of the fluid forcing. Adding additional higher-order predictors to the model does not fix the issue. Although our current neural networks model is good enough to capture the complex dynamics of both the structural mode and the hydrodynamic mode (Fig. 4), more sophisticated machine-learning models (e.g. long short-term memory network) may be helpful for predicting the system dynamics of extremely low-inertia wings.

In Fig. 6(c), we extend the data-driven approach to *swept* wings. A detailed description of the swept wing geometry and the characteristics of the associated nonlinear instabilities is reported by Zhu and Breuer (2023). Here we take the swept wing with a sweep angle $\Lambda = 15^\circ$ as an example. The wing inertia and damping are maintained at $I^* = 10.6$ and $b^* = 0.13$. Because the wing geometry has changed, all the training data has to be retaken and the ML model has to be retrained following the procedures discussed in §2.2 and §2.3. The Hopf point as well as the LCO amplitude after the Hopf point are precisely predicted. The ML model slightly underpredicts the LCO amplitude in the bistable region, and the saddle-node point is predicted to be at a slightly higher Ca as compared to experiments. Overall, the ML model is able to predict the system dynamics well for the swept wing, demonstrating the wide applicability of the proposed approach.

4. Discussions and Conclusion

In this study, we proposed and validated a data-driven approach for modeling large-amplitude aeroelastic oscillations of pitching wings. In the proposed approach, we trained a neural networks regression model to predict the nonlinear aerodynamic moment experienced by the wing based on the wing kinematics, namely the pitching angle, velocity, and acceleration. The training dataset was generated purely by one-way coupling prescribed motions and static measurements without any prior knowledge of the two-way coupling passive aeroelastic dynamics. The trained model was then combined with the aeroelastic governing equation and fed into an ordinary differential equation solver to simulate the passive aeroelastic system. “Virtual” experiments of high- and low-inertia wings were performed using the proposed method and the results were compared with physical experiments. The amplitude, frequency, and aerodynamic moment responses of the system were found to be well predicted by the proposed method, with the structural and hydrodynamic oscillation modes faithfully recreated. The unsteady growth and saturation of the pitching amplitude and the aerodynamic moment right after the bifurcation point were also successfully captured. Validations of the proposed approach on additional test cases demonstrated its high versatility. Due to the data-driven nature of this approach, the specific geometry of the elastically supported object does not come into play in the model, making this approach broadly applicable and easily adaptable to other aeroelastic systems.

The proposed data-driven approach successfully bridges one-way and two-way coupling fluid-structure interaction problems, opening up the possibility of using lower-cost, more accessible one-way coupling experiments/simulations to study higher-cost, less accessible two-way coupling FSI problems. More importantly and perhaps more excitingly, following the proposed approach, the excessive existing datasets of unsteady airfoils/wings with prescribed kinematics in the literature

can potentially be consolidated and used to train a more comprehensive data-driven model for studying more complex and realistic aeroelastic problems. The proposed approach also echoes the concept of “digital twins” (Jones et al., 2020), in a way that a “digital” aeroelastic system is created and trained using data obtained from its physical counterpart. And this “digital twin” can in turn be used to simulate and guide the study of the physical aeroelastic system.

We want to emphasize that the goal of the present study is to propose and validate a data-driven approach for modeling nonlinear aeroelastic systems, rather than to design and optimize a specific machine-learning model. We chose the three-layered neural networks model because it is simple to implement yet complex enough to capture the essential nonlinear dynamics of the unsteady aerodynamic moment. In fact, it is quite amazing that the highly nonlinear aerodynamic moment of pitching wings in massively-separated, vortex-dominated flows can be accurately predicted by the three very basic wing kinematics: pitching angle, velocity, and acceleration, without additional information about surface pressure or velocity field. Unfortunately, because the neural networks model is non-interpretable, it is difficult to infer any useful information from the model. Employing more interpretable machine-learning models such as SINDy (Brunton et al., 2016) might be able to provide more physical insights, but this lies out of the scope of the present study.

At the current stage, the proposed data-driven approach has been validated against large-amplitude flow-induced oscillations. It is not applicable to study small-amplitude aeroelastic instabilities such as laminar separation flutters (Negi et al., 2021). Additional small-amplitude oscillation data might be needed to train the model to predict those instabilities. Moreover, we see that the approach is not currently able to predict flow-induced oscillations of extremely low-inertia wings, although the high-inertia structural mode and the low-inertia hydrodynamic mode can both be accurately predicted. It is hypothesized that for extremely low-inertia wings, the system becomes too sensitive to the exact phase and amplitude of the fluid forcing. In addition, the neural networks model used in the proposed approach is a regression model, which means it is good at interpolating data. How good it is in extrapolating data (i.e. predicting aeroelastic dynamics beyond the amplitude and frequency range of the training data) remains a question for future studies. Lastly, the current work was only performed at a single Reynolds number, and for a particular wing geometry. Although we have previously shown that these nonlinear aeroelastic instabilities are generally insensitive to Reynolds number (Zhu et al., 2020), these effects are nevertheless important, and one would expect that the predictions of the fluid moment, and the details of the bifurcation points and oscillation amplitudes will change with Reynolds number, and thus will likely require additional input data and model training.

CRedit authorship contribution statement

Yuanhang Zhu: Conceptualization, Formal Analysis, Investigation, Methodology, Software, Validation, Visualization, Writing – original draft, Writing – review & editing. **Kenneth Breuer:** Conceptualization, Formal Analysis, Investigation, Methodology, Writing – review & editing.

Declaration of competing interest

The authors declare that they have no known competing financial interests or personal relationships that could have appeared to influence the work reported in this paper.

Data availability

Data will be made available on request.

Acknowledgments

This work was funded by the Air Force Office of Scientific Research, Grant FA9550-21-1-0462, managed by Dr. Gregg Abate.

Appendix A. Robustness test of the model

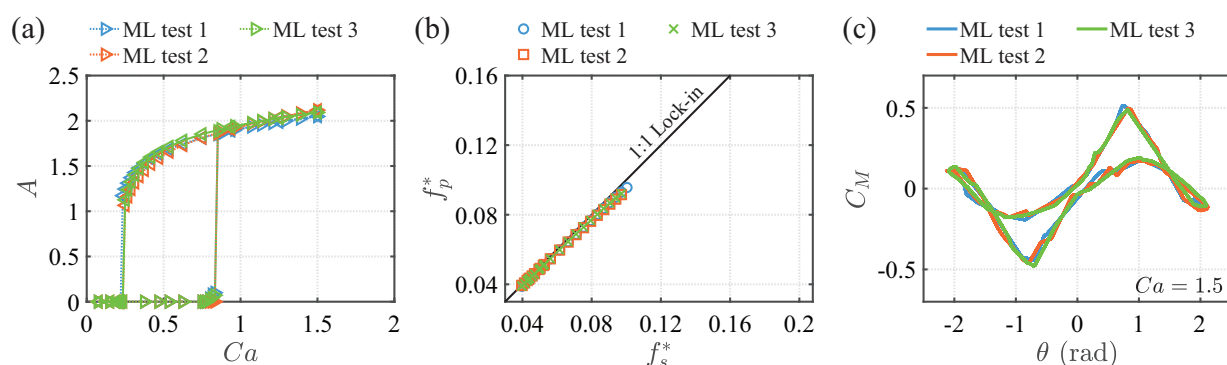


Figure A.7: Robustness test of the model using the high-inertia case, $I^* = 10.6$ and $b^* = 0.13$. The models are trained using the same neural networks structure but the training data is shuffled differently.

To test the robustness of the machine learning model, we repeat the high-inertia case of Fig. 4(a-c). We reshuffle the 580 dynamic and static cases of the training data (see §2.2) and use the reordered data to train the neural networks model. After retraining the model, we repeat the bifurcation tests, and the results are shown in Fig. A.7. The reshuffling and the retraining are repeated twice, corresponding to ML tests 2 and 3 in the figure. The results of Fig. 4(a-c) are replotted as ML test 1. We see that the amplitude, frequency, and aerodynamic moment response of the three ML tests are highly repeatable despite some small variations, demonstrating the high robustness of the model.

References

- Baik, Y.S., Bernal, L.P., Granlund, K., Ol, M.V., 2012. Unsteady force generation and vortex dynamics of pitching and plunging aerofoils. *J. Fluid Mech.* 709, 37–68.
- Bhat, S.S., Govardhan, R.N., 2013. Stall flutter of naca 0012 airfoil at low reynolds numbers. *J. Fluids Struct.* 41, 166–174.
- Brenner, M.P., Eldredge, J.D., Freund, J.B., 2019. Perspective on machine learning for advancing fluid mechanics. *Phys. Rev. Fluids* 4, 100501.
- Brunton, S.L., Noack, B.R., Koumoutsakos, P., 2020. Machine learning for fluid mechanics. *Annu. Rev. Fluid Mech.* 52, 477–508.
- Brunton, S.L., Proctor, J.L., Kutz, J.N., 2016. Discovering governing equations from data by sparse identification of nonlinear dynamical systems. *Proc. Natl. Acad. Sci.* 113, 3932–3937.

- Carter, D.W., Ganapathisubramani, B., 2023. Low-order modeling and sensor-based prediction of stalled airfoils at moderate reynolds number. *AIAA J.* 61, 2893–2905.
- Chen, D., Kaiser, F., Hu, J., Rival, D.E., Fukami, K., Taira, K., 2023. Sparse pressure-based machine learning approach for aerodynamic loads estimation during gust encounters. *AIAA J.* , 1–16.
- Clements, R.R., Maull, D.J., 1975. The representation of sheets of vorticity by discrete vortices. *Prog. Aerosp. Sci.* 16, 129–146.
- Cybenko, G., 1989. Approximation by superpositions of a sigmoidal function. *Math. Control. Signals, Syst.* 2, 303–314.
- Dimitriadis, G., 2017. Introduction to nonlinear aeroelasticity. John Wiley & Sons.
- Dimitriadis, G., Li, J., 2009. Bifurcation behavior of airfoil undergoing stall flutter oscillations in low-speed wind tunnel. *AIAA J.* 47, 2577–2596.
- Dowell, E., Edwards, J., Strganac, T., 2003. Nonlinear aeroelasticity. *J. Aircraft* 40, 857–874.
- Dowell, E.H., Curtiss, H.C., Scanlan, R.H., Sisto, F., 1989. A modern course in aeroelasticity. Springer.
- Dowell, E.H., Hall, K.C., 2001. Modeling of fluid-structure interaction. *Annu. Rev. Fluid Mech.* 33, 445–490.
- Dugundji, J., 2008. Some aeroelastic and nonlinear vibration problems encountered on the journey to ithaca. *AIAA J.* 46, 21–35.
- Eldredge, J.D., Jones, A.R., 2019. Leading-edge vortices: mechanics and modeling. *Annu. Rev. Fluid Mech.* 51, 75–104.
- Ford, C.W.P., Babinsky, H., 2013. Lift and the leading-edge vortex. *J. Fluid Mech.* 720, 280–313.
- Fukami, K., Taira, K., 2023. Grasping extreme aerodynamics on a low-dimensional manifold. *Nat. Commun.* 14, 6480.
- Gabbai, R.D., Benaroya, H., 2005. An overview of modeling and experiments of vortex-induced vibration of circular cylinders. *J. Sound Vib.* 282, 575–616.
- Garrick, I.E., 1936. Propulsion of a flapping and oscillating airfoil. Technical Report 567. NACA.
- Goza, A., Colonius, T., 2017. A strongly-coupled immersed-boundary formulation for thin elastic structures. *J. Comput. Phys.* 336, 401–411.
- Graff, J., Medina, A., Lagor, F.D., 2023. Information-based sensor placement for data-driven estimation of unsteady flows. *AIAA J.* 61, 4864.
- Hickner, M.K., Fasel, U., Nair, A.G., Brunton, B.W., Brunton, S.L., 2023. Data-driven unsteady aeroelastic modeling for control. *AIAA J.* 61, 780–792.
- Jones, D., Snider, C., Nassehi, A., Yon, J., Hicks, B., 2020. Characterising the digital twin: A systematic literature review. *CIRP J. Manuf. Sci. Technol.* 29, 36–52.
- Katz, J., 1981. A discrete vortex method for the non-steady separated flow over an airfoil. *J. Fluid Mech.* 102, 315–328.
- Khalak, A., Williamson, C.H.K., 1996. Dynamics of a hydroelastic cylinder with very low mass and damping. *J. Fluids Struct.* 10, 455–472.
- Kou, J., Zhang, W., 2021. Data-driven modeling for unsteady aerodynamics and aeroelasticity. *Prog. Aerosp. Sci.* 125, 100725.
- Larsen, A., 1998. Advances in aeroelastic analyses of suspension and cable-stayed bridges. *J. Wind. Eng. Ind. Aerodyn.* 74, 73–90.
- Lee, H., Simone, N., Su, Y., Zhu, Y., Ribeiro, B.L.R., Franck, J.A., Breuer, K., 2022. Leading edge vortex formation and wake trajectory: Synthesizing measurements, analysis, and machine learning. *Phys. Rev. Fluids* 7, 074704.
- Liu, T., Wang, S., Zhang, X., He, G., 2015. Unsteady thin-airfoil theory revisited: application of a simple lift formula. *AIAA J.* 53, 1492–1502.
- McCroskey, W.J., 1982. Unsteady airfoils. *Annu. Rev. Fluid Mech.* 14, 285–311.
- Menon, K., Mittal, R., 2019. Flow physics and dynamics of flow-induced pitch oscillations of an airfoil. *J. Fluid Mech.* 877, 582–613.
- Menon, K., Mittal, R., 2021. Quantitative analysis of the kinematics and induced aerodynamic loading of individual vortices in vortex-dominated flows: a computation and data-driven approach. *J. Comput. Phys.* 443, 110515.
- Mishra, V., Crawford, C., Buckham, B., 2023. Predicting hydrodynamic forces on heave plates using a data-driven modelling architecture. *J. Fluids Struct.* 116, 103812.

- Morse, T.L., Williamson, C.H.K., 2009. Prediction of vortex-induced vibration response by employing controlled motion. *J. Fluid Mech.* 634, 5–39.
- Negi, P.S., Hanifi, A., Henningson, D.S., 2021. On the onset of aeroelastic pitch-oscillations of a naca0012 wing at transitional reynolds numbers. *J. Fluids Struct.* 105, 103344.
- Onoue, K., Breuer, K.S., 2016. Vortex formation and shedding from a cyber-physical pitching plate. *J. Fluid Mech.* 793, 229–247.
- Onoue, K., Song, A., Strom, B., Breuer, K.S., 2015. Large amplitude flow-induced oscillations and energy harvesting using a cyber-physical pitching plate. *J. Fluids Struct.* 55, 262–275.
- Ōtomo, S., Henne, S., Mulleners, K., Ramesh, K., Viola, I.M., 2021. Unsteady lift on a high-amplitude pitching aerofoil. *Exp. Fluids* 62, 1–18.
- Raissi, M., Perdikaris, P., Karniadakis, G.E., 2019. Physics-informed neural networks: A deep learning framework for solving forward and inverse problems involving nonlinear partial differential equations. *J. Comput. Phys.* 378, 686–707.
- Ramesh, K., Gopalarathnam, A., Granlund, K., Ol, M.V., Edwards, J.R., 2014. Discrete-vortex method with novel shedding criterion for unsteady aerofoil flows with intermittent leading edge vortex shedding. *J. Fluid Mech.* 751, 500–538.
- Ribeiro, B.L.R., Franck, J.A., 2023. Machine learning to classify vortex wakes of energy harvesting oscillating foils. *AIAA J.* 61, 1281–1291.
- Siddiqui, M.F., De Troyer, T., Decuyper, J., Csurscia, P.Z., Schoukens, J., Runacres, M.C., 2022. A data-driven nonlinear state-space model of the unsteady lift force on a pitching wing. *J. Fluids Struct.* 114, 103706.
- Strogatz, S.H., 1994. *Nonlinear Dynamics and Chaos: With Applications to Physics, Biology, Chemistry, and Engineering*. Perseus Books.
- Su, Y., Breuer, K.S., 2019. Resonant response and optimal energy harvesting of an elastically mounted pitching and heaving hydrofoil. *Phys. Rev. Fluids* 4, 064701.
- Theodorsen, T., 1935. General theory of aerodynamic instability and the mechanism of flutter. Technical Report 496. NACA.
- Wang, C., Eldredge, J.D., 2013. Low-order phenomenological modeling of leading-edge vortex formation. *Theor. Comp. Fluid Dyn.* 27, 577–598.
- Wang, J., Geng, L., Ding, L., Zhu, H., Yurchenko, D., 2020. The state-of-the-art review on energy harvesting from flow-induced vibrations. *Appl. Energy* 267, 114902.
- Williamson, C.H.K., Govardhan, R., 2004. Vortex-induced vibrations. *Annu. Rev. Fluid Mech.* 36, 413–455.
- Williamson, C.H.K., Govardhan, R., 2008. A brief review of recent results in vortex-induced vibrations. *J. Wind. Eng. Ind. Aerodyn.* 96, 713–735.
- Xia, X., Mohseni, K., 2013. Lift evaluation of a two-dimensional pitching flat plate. *Phys. Fluids* 25.
- Xiao, Q., Zhu, Q., 2014. A review on flow energy harvesters based on flapping foils. *J. Fluids Struct.* 46, 174–191.
- Young, J., Lai, J.C.S., Platzer, M.F., 2014. A review of progress and challenges in flapping foil power generation. *Prog. Aerosp. Sci.* 67, 2–28.
- Zhu, Y., Breuer, K., 2023. Flow-induced oscillations of pitching swept wings: stability boundary, vortex dynamics and force partitioning. *J. Fluid Mech.* 977, A1.
- Zhu, Y., Mathai, V., Breuer, K., 2021. Nonlinear fluid damping of elastically mounted pitching wings in quiescent water. *J. Fluid Mech.* 923, R2.
- Zhu, Y., Su, Y., Breuer, K., 2020. Nonlinear flow-induced instability of an elastically mounted pitching wing. *J. Fluid Mech.* 899, A35.